Gondwana Research xxx (2015) xxx–xxx

Contents lists available at ScienceDirect

Gondwana Research

journal homepage: www.elsevier.com/locate/gr

Crustal shear-wave velocity structure of northeastern Tibet revealed by ambient seismic noise and receiver functions

Zhenbo Wu [a,b], Tao Xu [a,c,*], José Badal [d], Huajian Yao [e,f], Chenglong Wu [a,b], Jiwen Teng [a]

[a] State Key Laboratory of the Lithosphere Evolution, Institute of Geology and Geophysics, Chinese Academy of Sciences, Beijing 100029, China
[b] University of Chinese Academy of Sciences, Beijing 100049, China
[c] CAS Center for Excellence in Tibetan Plateau Earth Sciences, Beijing 100101, China
[d] Physics of the Earth, Sciences B, University of Zaragoza, Pedro Cerbuna 12, 50009 Zaragoza, Spain
[e] Laboratory of Seismology and Physics of Earth's Interior, School of Earth and Space Sciences, University of Science and Technology of China, Hefei 230026, China
[f] National Geophysical Observatory at Mengcheng, Anhui, China

ARTICLE INFO

Article history:
Received 27 March 2015
Received in revised form 9 August 2015
Accepted 14 August 2015
Available online xxxx

Keywords:
Northeastern Tibet
Ambient noise cross-correlation
Phase velocity dispersion
Receiver functions
Joint inversion
Crustal low velocity zone

ABSTRACT

The Tibetan plateau is formed by the persistent convergence between the Indian and Eurasian plates. The northeastern Tibetan plateau is undergoing young deformation that has been noticed for a long time. We conduct a passive-source seismic profile with 22 stations in NE Tibet in order to investigate the crustal shear-wave velocity structure and its relationship with tectonic processes. In this paper we obtain the Rayleigh-wave phase velocity dispersion data among all station pairs within the period bandwidth of 5–20 s from the method of ambient noise cross-correlations. Phase velocity variations correlate well with surface geological boundaries and tectonic features, for instance, low phase velocity beneath the Songpan–Ganzi block and the Guide basin. We also compute P-wave receiver functions based on the selected teleseismic events with similar ray parameters, and perform the joint inversion of surface wave dispersion data and receiver functions to obtain the 2-D crustal shear-wave velocity structure along the profile. The inversion results show that low shear-wave velocities beneath the Songpan–Ganzi block are widespread in the middle-to-lower crust. In together with high crustal *Vp/Vs* ratios and high temperature suggested by the P-wave velocities obtained from the active-source seismic study, we suggest that the low velocity zone beneath the Songpan–Ganzi block is probably attributed to partial melting. Across the North Kunlun fault, there is no crustal LVZ found beneath the Kunlun block. This structural difference may have already existed before the collision of the two blocks, or due to limit of the northward extension for the crustal LVZ across the North Kunlun fault.

1. Introduction

Uplift of the Tibetan plateau is the most spectacular tectonic event during the Cenozoic created by the collision of India and Eurasia. Fundamental questions persist concerning the initiation of the convergence (e.g., Molnar and Tapponnier, 1975; Rowley, 1996; Aitchison et al., 2011; Sun et al., 2012; Zhang et al., 2012; Hu et al., 2015) and the mechanism of lithospheric deformation (e.g., Tapponnier and Molnar 1976; England and Houseman, 1989; Royden et al., 1997; Replumaz et al., 2014; Chen et al., 2015). Many models have been proposed to explain its dynamic responses to collision and its consequent deformation patterns. To this respect, three models have received wide attention, that is, the rigid block extrusion (Tapponnier and Molnar 1976; Tapponnier et al., 1982), the thin-viscous-sheet model (England and Houseman, 1986, 1989), and the crustal channel flow model (Royden et al., 1997).

The northeastern (NE) Tibetan plateau, viewed as a young outgrowth of its evolution and deformation (Meyer et al., 1998), has been a focus of many studies (e.g., Galvé et al., 2002; Vergne et al., 2002; Clark et al., 2010; Duvall and Clark, 2010; Karplus et al., 2013; Tian and Zhang, 2013; Xia et al., 2011; Deng et al., 2015). Deformation mechanisms that work here at present may resemble what happened in the central plateau and participated in the formation of the Tibetan plateau. This is one of the motivations for this study, which will help us understand the earlier deformation of central Tibet. On the other hand, some studies in the southeastern (SE) Tibetan plateau have found that low shear-wave velocities exist in the middle-to-lower crust (Yao et al., 2008, 2010; Liu et al., 2014). We are concerned about whether this phenomenon also exists in the NE Tibetan plateau. It will be very helpful to understand how the eastward expansion of the Tibetan plateau material is bifurcated by the rigid Sichuan Basin on the basis of comparing deformation patterns in the NE and SE Tibetan plateaus. Many works have been done from different perspectives

* Corresponding author at: State Key Laboratory of the Lithosphere Evolution, Institute of Geology and Geophysics, Chinese Academy of Sciences, Beijing 100029, China.
E-mail address: xutao@mail.iggcas.ac.cn (T. Xu).

http://dx.doi.org/10.1016/j.gr.2015.08.009
1342-937X/

to discuss this issue. There may exist a mechanically weak lower crust that accounts for crustal channel flow in the surrounding regions of the Sichuan Basin (Clark and Royden, 2000). Resistivity models obtained from magnetotelluric data show evidences for penetration of partial melting crust across the Kunlun Fault into northern Tibet (Pape et al., 2012).

Galvé et al. (2002) collect the wide-angle reflection–refraction data by active-source seismic survey. The obtained P- and S-wave velocities support predominant felsic composition for the crust and suggest that only the upper crust has been thickened to the north of the Kunlun fault; to the south of this fault the thicker crust is composed by two layers, which could be the superposition of the originally thin crust of the Bayar Har Terrane on the lower crust of the domain to the north. However, Liu et al. (2006) suggest that crustal thickening mainly happens in the lower crust in the NE Tibetan plateau, based on the Darlag–Lanzhou–Jingbian seismic refraction profile.

Seismic interferometry technique using ambient seismic noise has rapidly become an important method to investigate the Earth structure at different scales. In fact, surface wave tomography based on the ambient noise method has provided essential constraints on crustal structure in the world (e.g. Shapiro et al., 2005; Yao et al., 2010; Zheng et al., 2011; Badal et al., 2013). Ambient-noise tomography results of northern Tibet based on INDEPTH-IV data (Yang et al., 2012; Karplus et al., 2013) show that the low velocities are widely distributed in the mid-lower crust of the Tibetan plateau. However, Poisson's ratio observations provided by a series of passive-source seismic surveys reveal more felsic composition of the whole crust and suggest that the upper crust is thickened to accommodate the north–south shortening from the collision of the India–Eurasia plates (Vergne et al., 2002; Jiang et al., 2006; Zhang et al., 2011; Xu et al., 2014).

In this study, we use the continuous ambient noise data as well as teleseismic P-wave data from a passive-source seismic experiment (a linear array with 22 stations) in the NE Tibetan plateau. We perform a joint inversion of short-period Rayleigh wave phase dispersion data from ambient noise tomography and P-wave receiver functions to construct the 2-D crustal shear-wave velocity structure beneath the array profile. Finally we discuss the tectonic implications of the crustal structure obtained in this study.

2. Tectonic setting

The inset in Fig. 1a denotes the study area in the NE Tibetan plateau and shows the northeast–southwest trending seismograph stations deployed between the cities of Xining (to the north) and Moba (to the south). The passive-source seismic survey line crosses the Songpan–Ganzi block and Kunlun block, and reaches the southern edge of the Qilian block from south to north. Regional tectonic characteristics are quite complicated, including several intracontinental sutures, strike-slip faults, thrust faults and Cenozoic basins (Fig. 1b). Here we briefly introduce them in the following content.

2.1. Songpan–Ganzi Block

The easternmost part of Songpan–Ganzi block is a roughly triangular-shaped tectonic unit surrounded by the Kunlun block to the north, the Qiangtang block to the south and the Sichuan Basin to the east (Fig. 1a). It is an ancient remnant ocean basin filled by Triassic turbidite sediments with thickness over 10 km, which is a witness of the evolutive history and deformation undergone in the adjacent blocks such as Qiangtang, east Kunlun, North China, western Qingling blocks, and even the Qinling–Tongbai–Hong'an–Dabie formation located several hundred kilometers to the east (Enkelmann et al., 2007). The closure of the Songpan–Ganzi remanent ocean during the Triassic to Early Jurassic partially sank the Songpan–Ganzi terrane beneath the Kunlun arc along the Animaqing–Kunlun–Muztagh suture (Burchfiel et al., 1995; Yin and Harrison, 2000). The eastern boundary of the Songpan–Ganzi Terrane meets the western edge of the Late Triassic/Early Jurassic Longmenshan thrust belts, which lies along the western edge of the South China (Yangtze) craton (Burchfiel et al., 1995; Zhang et al., 2010). Triassic strata overlies the Paleozoic shallow marine sequences of South China (Burchfiel et al., 1995), which suggests that a slope–shelf transition overlies a continental basement, at least in the easternmost part of the Songpan–Ganzi block (Yin and Harrison, 2000).

2.2. Kunlun Block

The Kunlun and Songpan–Ganzi blocks are separated by the Kunlun strike-slip fault, which probably began left-lateral slipping since ~10 Ma ago (Fu and Awata, 2007; Clark et al., 2010) and partially follows the trace of the Animaqing–Kunlun–Muztagh suture (Fig. 1b). This fault has already provoked five $Mw > 7.0$ earthquakes in the past century and more recently the 11/14/2001 Mw 8.1 Hoh Xil earthquake that results in a 430-km-long surface rupture. These earthquakes indicate that the Kunlun fault is still keeping active. GPS measurements along the Kunlun fault (Duvall and Clark, 2010) support that the deformation from the continental collision dissipates northward rather than eastward in the NE Tibetan plateau. The similar conclusion has been made based on shear-wave splitting parameters obtained from the previous work (see Fig. 7 in Chen et al., 2015).

The Kunlun fault, as a major sinistral strike-slip fault in the NE Tibetan plateau, plays an important role on the northward growth of Tibet. Many geophysical studies have been conducted to observe how the lithosphere of microcontinent plates deforms from the relative motions among different rigid blocks. However, how the blocks have been contacted along the Kunlun fault is still under debate, and both northward subduction and southward subduction beneath the plateau have been suggested (Yin and Harrison, 2000; Tapponnier et al., 2001; Kind et al., 2002; Zhang et al., 2010).

Further north, South Qilian suture separates the Kunlun block from the Qilian block (Fig. 1b). Previous tectonic studies indicate that the Qilian Shan thrust belt collides with the Qaidam–Kunlun block during the Early Paleozoic (Yu et al., 2012). The Kunlun block develops a series of intracontinental strike-slip faults and thrust faults, and most of them are younger than 10 Ma (Clark et al., 2010). The study of average slip rates for the Elashan and Riyue Shan faults, two north-northwest-trending dextral strike-slip faults, west and east of the Qinghai Lake, clearly shows the tectonic deformation in the northeastern margin of the Tibetan plateau since ca. 8–12 Ma (Yuan et al., 2011). The intramontane basins such as the Gonghe–Guide basin and the Xining basin are strongly controlled by these regional faults. The Gonghe–Guide basin is a typical intramontane sedimentary basin similar to the larger Qaidam basin to the west. The course of the Yellow River and its tributaries has exposed a rather complete Neogene sequence (Fang et al., 2005). Further north the Xining subbasin of the Langzhou basin has the largest and continuous Cenozoic sedimentary layer (Dai et al., 2006). Usually, these Cenozoic basins at the northeastern margin of the Tibetan plateau preserve the important stratigraphic records that provide the evidence of the deformation and evolution of this area.

3. Data acquisition

With the purpose on probing the response of the India–Eurasia tectonic collision in the NE Tibetan plateau, we conduct a passive-source seismic experiment between Xining and Moba (Fig. 1a) from November 2010 to June 2011, using 22 seismograph stations with Reftek-72A data loggers and Guralp CMG3-ESP sensors with bandwidths 0.02–30 s or 60 s. The station spacing is about 10 to 15 km (Fig. 1b). Stations S00–S01 are installed in the Qilian block, S02–S16 in the Kunlun block and S17–S27 in the Songpan–Ganzi block. Three-component ground movements are recorded with 40s sample-per-second (sps) at each station.

Please cite this article as: Wu, Z., et al., Crustal shear-wave velocity structure of northeastern Tibet revealed by ambient seismic noise and receiver functions, Gondwana Research (2015), http://dx.doi.org/10.1016/j.gr.2015.08.009

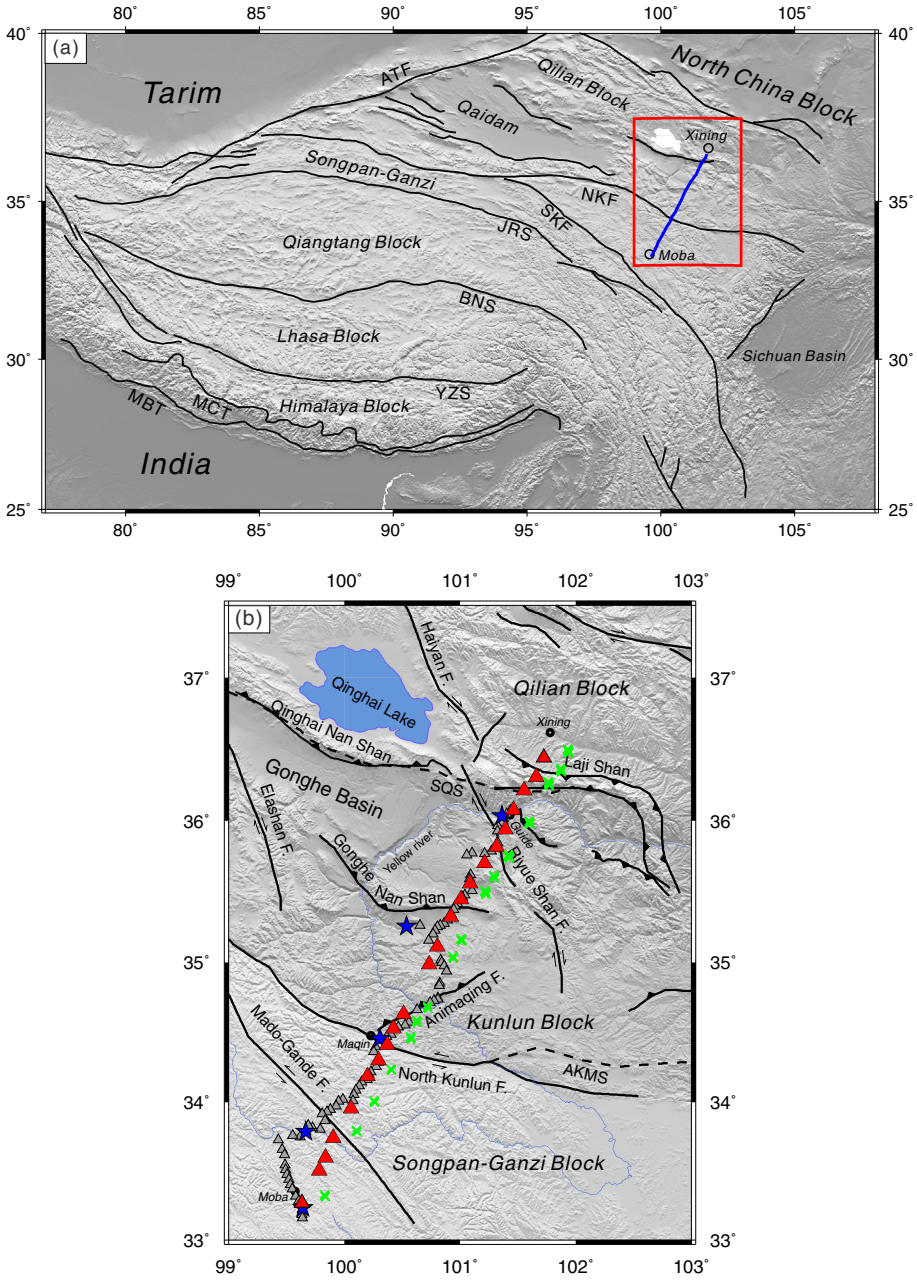

Fig. 1. (a) Tectonic map of the Tibetan plateau and surrounding areas. The red box shows the study region in northeastern Tibet and the seismic array deployed between the cities of Xining (to the north) and Moba (to the south). (b) Zoom-in view of the study area and location of the passive-source seismic survey line. Red triangles denote the seismic broad-band stations used in this study. Gray triangles and blue stars denote the seismic receivers and shots fired in the active-source seismic experiment (Zhang et al., 2011). Green crosses denote the piercing points at the depth 60 km of the calculated receiver functions. Acronyms for sutures and faults: YZS, Indus–Zangbo suture; BNS, Bangong–Nujiang suture; JRS, Jinsha suture; AKMS, Animaqing–Kunlun–Muztagh suture; SQS, South Qilian suture; SKF, South Kunlun fault; NKF, North Kunlun fault; ATF, Altyn–Tagh fault; MCT, main central thrust; MBT, main boundary thrust. (For interpretation of the references to color in this figure legend, the reader is referred to the web version of this article.)

In order to avoid any ambiguity arising from propagation effects caused by different ray paths and unequal anisotropic properties from different azimuths, we select teleseismic events located in the West Pacific subduction zone near Japan to compute the receiver functions, these events have similar back azimuths and ray parameters (Fig. 2).

4. Method

Deep structure along this seismic survey line has been studied in two ways: the wide-angle reflection–refraction (Zhang et al., 2011) and the receiver function imaging (Xu et al., 2014). However, the steeply incident body waves used in the wide-angle reflection–refraction are less sensitive to the shallow heterogeneity than dispersion curves of short-period surface waves, and usually it is hard to obtain the high resolution shear-wave velocity structure mainly due to the low signal-to-noise ratio (SNR) of shear-wave data. Receiver function is good at detecting interfaces with a large velocity contrast, but it is less sensitive to the absolute value of wave speed. We combine dispersion curves of short-period surface waves from ambient noise cross-correlation and teleseismic P-wave receiver functions together to obtain the high resolution shear-wave velocity structure in the crust.

4.1. Surface wave empirical Green's functions

Based on an assumption of randomly distributed ambient noise sources, monthly or longer continuous data can be cross-correlated to

compute the surface wave empirical Green's functions (EGFs) with sufficient SNR for dispersion analysis and to produce reliable tomographic images (Shapiro et al., 2005; Yao et al., 2006; Bensen et al., 2007).

A series of preprocessing steps should be applied to the waveform data to improve the SNR of the EGFs. Commonly, the ambient seismic data preprocessing consists of band-pass filtering, in our case using the bandwidth 0.2–50 s, cutting the continuous data to one day length, de-trending the zero line slope, removing instrument response, and re-sampling the data to improve the computational efficiency, and in our case from 40 sps to 10 sps, normalization in time domain and spectral whitening in frequency domain (Bensen et al., 2007; Badal et al., 2013). Cross-correlations of ambient seismic noise would be seriously contaminated by the local or teleseismic events without the normalization in the time domain. On the other hand, since the amplitude spectrum of ambient seismic noise is normally not flat in the frequency domain, we use a spectral whitening technique to smooth the amplitude spectrum. This operation can produce comparable amplitudes for the concerned frequency band and mute the influence from the persistent monochromatic seismic sources (Villaseñor et al., 2007; Zheng et al., 2011).

Cross-correlations of vertical-component ambient seismic noise are calculated for each available station pair of the 22 stations using the daily time series, and the cross-correlations consist of positive and negative lags with apparent Rayleigh wave signals. Fig. 3 shows the stacked cross-correlation functions (CFs) in the frequency band 10–20 s extracted from ambient noise cross-correlations with a total of 152-day record between the stations S06 and S17. The difference between Fig. 3(a) and (b) is that the result plotted in (a) is computed without spectral whitening in frequency domain but for (b) with spectral whitening. The latter one has a markedly increased SNR as expected. A common phenomenon is that the causal and acausal parts of the CFs are asymmetric in amplitude but nearly symmetric in travel time (Fig. 3a–b). This is probably due to inhomogeneous distribution of ambient noise sources and the attenuation that mainly affects the signal amplitude (Stehly et al., 2006). Zheng et al. (2011) point out that most EGFs between stations in north China are disturbed by a persistent localized microseismic source on the Kyushu Island. In our study, the EGFs extracted from

Fig. 2. Global map showing the selected earthquakes (green circles) for calculating receiver functions, which are located roughly in the same area and have similar epicentral distances (around 35°), back azimuths and ray parameters. The red triangle indicates the approximate location of the seismic array. (For interpretation of the references to color in this figure legend, the reader is referred to the web version of this article.)

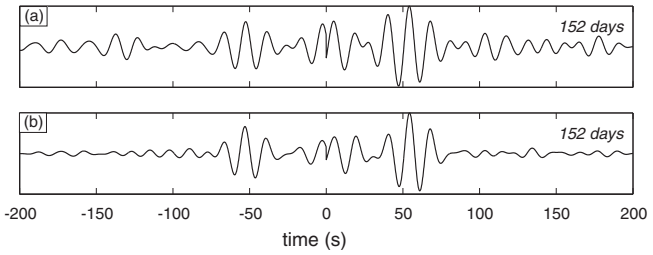

Fig. 3. (a)–(b) Daily cross-correlation functions within the period band 10–20 s after being stacked for a total of 152 days between the stations S06 and S17. The difference is that the former (a) is computed without spectral whitening, while the latter (b) is the result with spectral whitening. SNR increases markedly in the latter case.

the time-derivative of CFs emerge clear surface wave signals without the existence of undesired signals in the time window shown as Fig. 4. So we think the asymmetric amplitudes are mainly caused by the inhomogeneous distribution of noise sources. To obtain the reliable dispersion measurement, the positive and negative EGF signals are averaged to create symmetric components (Bensen et al., 2007; Yang et al., 2007).

There are a total of 231 EGFs obtained from all possible station pairs. Fig. 4a shows the stacked EGFs within the period band 10–20 s between the station S00 and all other stations during the recording period. Fig. 4b shows the daily EGFs corresponding to the station pair S02–S11, and the stacked trace is showed as the heavy solid line on the top. As we can see, the recovered surface wave signal is quite stable.

4.2. Phase velocity dispersion mapping

We measure the phase velocity dispersion curves from the EGFs based on a far-field approximation and an image transformation technique (Yao et al., 2006). There are two constraints to be satisfied: one is that the distance between station pair has to be at least three wavelengths of the surface wave signal in order to satisfy the far-field approximation; the other is that the SNR has to be greater than 5 to ensure the reliability of phase velocity measurements. Here SNR is defined as the ratio of the maximum amplitude of the signal window and the mean envelope amplitude of the 150 s long noise window right after the signal window around the central period. As an example, the EGF extracted from the data at two stations (Fig. 5a) is shown in Fig. 5b, the SNR value is shown in Fig. 5c. Fig. 5d shows the velocity-period image and the red circles represent the measured phase velocities within the period band 5–20 s.

In order to ensure the reliability of the measurements, we repeat the above process for different monthly data of each station pair. The dispersion curves with significant discrepancies from most of the results are discarded. We measure the Rayleigh-wave phase velocity dispersion curves for all possible station pairs and finally obtain 89 dispersion curves at periods from 5 to 20 s. These curves are plotted together in Fig. 5e. Both the average phase velocity dispersion curve and its standard deviation at different periods are shown in Fig. 5f.

We use the continuous regionalization and the generalized inversion scheme to invert path-averaged phase velocities at each period for 2-D phase velocity distribution (Tarantola and Valette, 1982; Montagner, 1986; Yao et al., 2010). We set a proper 2D inversion region containing our survey line and the grid interval used for inversion is 0.5° × 0.5°. Yao et al. (2010) introduce the details about this scheme that include inversion for both isotropic phase velocities and azimuthal anisotropy. Here, we are only concerned of the isotropic phase velocity variation. For each period, we first obtain period-dependent 2D phase velocity variations. Then we interpolate the phase velocity maps of different periods to the station locations along the survey line. The short-period phase velocities are very sensitive to the shallow geological features.

Please cite this article as: Wu, Z., et al., Crustal shear-wave velocity structure of northeastern Tibet revealed by ambient seismic noise and receiver functions, Gondwana Research (2015), http://dx.doi.org/10.1016/j.gr.2015.08.009

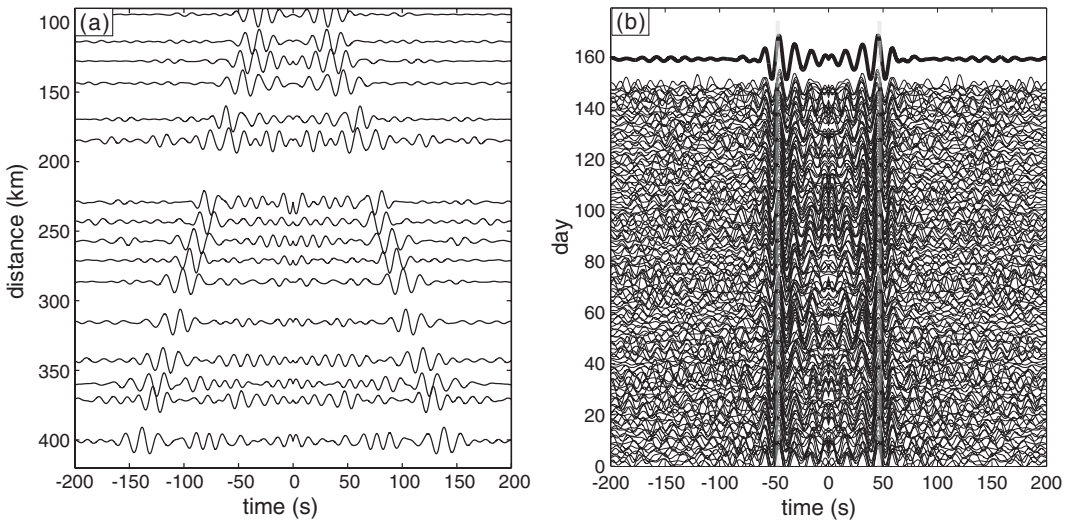

Fig. 4. (a) Symmetric EGFs extracted from the daily cross-correlations of the vertical component data recorded at the station S00 with the other stations, stacked within the period band 10–20 s and sorted from top to bottom by the interstation distance. (b) Daily EGFs for a single station pair S02–S11. The stacked trace for all daily EGFs is shown as the heavy solid line on top.

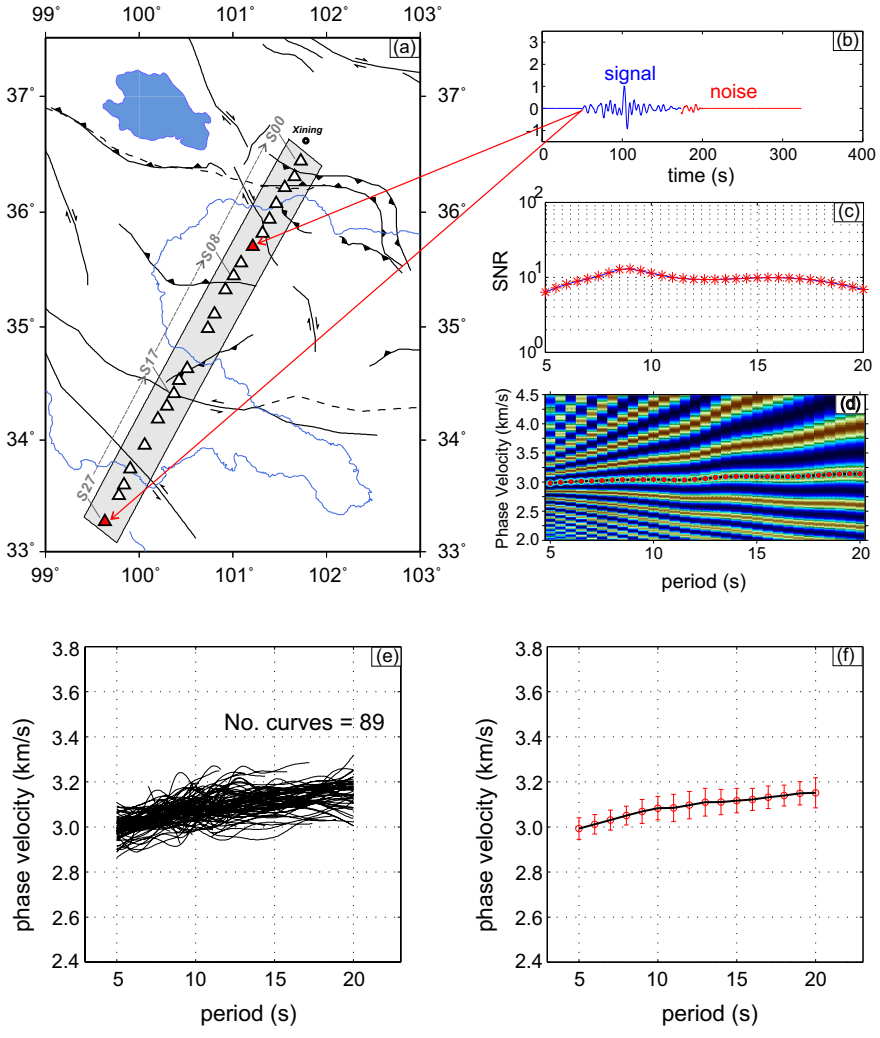

Fig. 5. (a) Passive-source seismic array deployed in northeastern Tibet (triangles) that is used in this study. (b) EGF for the station pair S06–S27 (red triangles). (c) Signal-to-noise ratio (SNR) versus period for the EGF in (b). (d) Velocity-period diagram and the selected phase velocity dispersion curve (red dotted line) within the phase velocity window 2.0–4.5 km/s at periods 5–20 s. (e) All 89 phase velocity dispersion curves measured from EGFs. (f) Averaged phase velocity dispersion curve with vertical bars representing the standard deviations at different periods. (For interpretation of the references to color in this figure legend, the reader is referred to the web version of this article.)

Please cite this article as: Wu, Z., et al., Crustal shear-wave velocity structure of northeastern Tibet revealed by ambient seismic noise and receiver functions, Gondwana Research (2015), http://dx.doi.org/10.1016/j.gr.2015.08.009

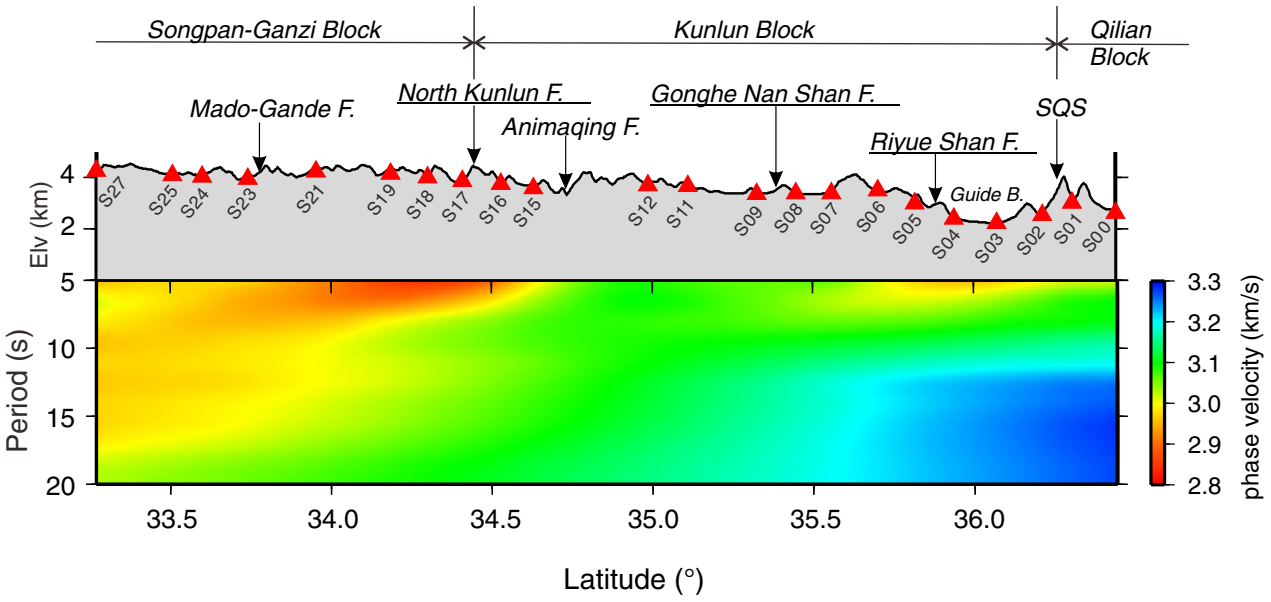

Fig. 6. Rayleigh-wave phase velocities versus periods along the seismic array. On top: surface topography along the survey line with the elevation decreasing very smoothly from south to north, and geographic location of the array stations (red triangles). The faults in Fig. 1b are also indicated here. (For interpretation of the references to color in this figure legend, the reader is referred to the web version of this article.)

As it can be seen in Fig. 6, the spatial distribution of phase velocity along the survey line is correlated with the surface tectonic features. Phase velocities as low as 2.8 km/s at periods of 5–8 s appear in the vicinity of the North Kunlun fault, a zone crossed by strike-slip and thrust faults. The cause of these low velocities is associated with the Triassic turbidite sediments in the Songpan–Ganzi block. At greater periods, phase velocities close to 3.0 km/s appear under the southernmost transect of the survey line and stretch northward up to the North Kunlun fault. In the southern Kunlun block, there shows a uniform phase velocity of ~3.1 km/s. Across the Gonghe Nan Shan fault, the phase velocity changes from 3.2 km/s between the Gonghe Nan Shan and Riyue Shan faults to 3.3 km/s northward of the Qilian block. However, velocities as low as 2.9–3.0 km/s at periods of 5–8 s appear again in the Guide basin, between the Riyue Shan fault and the South Qilian suture.

4.3. Receiver functions

We compute P-wave receiver functions by iterative deconvolution of the vertical component from the radial component from these selected events in the time domain (Ligorría and Ammon, 1999). As shown in Fig. 1b with green cross symbols, the piercing points at 60 km depth (average Moho depth) of these receiver functions parallel the survey line, which indicates that the shear-wave velocity structures constrained by these receiver functions are capable of representing the shear-wave structures of the study area. On the other hand, the piercing points of each station are almost overlapped, which indicates that the receiver functions have similar travel time for the P-to-S converted phases and allow us to stack them by a simple linear scheme. However, if we use all global events to compute the receiver functions, the move-out technique must be applied before stacking. The move-out value could be relatively large and produce artificial errors when the individual epicentral distance of the event is far away from the reference epicentral distance. We have totally avoided this disadvantage by only selecting the events located in the same region. In Fig. 7a we show the receiver functions with the Gaussian coefficient 1.0 for the selected events at the station S04 and the stacked result is plotted on the top. In Fig. 7b we arrange these stacked results for all stations along the survey line and sketch the Moho structure from south to north.

5. Joint inversion of surface wave dispersion and receiver function

5.1. Implementation

Receiver functions dominated by P-to-S converted phases can provide good constraints for the shear-wave velocity discontinuities of the Earth, and surface wave dispersion can provide constraints on the average shear-wave velocities in different depth ranges. Joint inversion of these two data sets can provide much better constraints on the crustal shear-wave velocity structure beneath our survey line.

We perform a damped least-squares scheme (Tarantola and Valette, 1982) and follow the joint inversion procedure based on the minimization of an objective function including both surface wave dispersion data and receiver functions (Julià et al., 2000). The computer program package developed by Herrmann and Ammon (2004) is used to obtain the 1-D shear-wave velocity structure for each station. According to the least-squares scheme, we shall provide an initial shear velocity model as accurate as possible to greatly reduce the non-uniqueness of the inversion results. Here we interpolate a 3D *Vsv* model of the crust and uppermost mantle beneath Tibet from ambient noise tomography provided by Yang et al. (2012) as our initial shear wave velocity model. We calculate the P-wave velocity based on the *Vp*/*Vs* ratio given by the previous receiver function study (Xu et al., 2014). Then, we determine the density by using the empirical formula $\rho = 0.77 + 0.32Vp$. The initial model is parameterized by thin layers with 1 km thickness to get an almost continuous velocity model with depth to avoid interfaces from sharply changed velocities (Ammon, et al., 1990).

The objective function that we minimize is shown as follows:

$$s = \frac{(1-p)}{N_r}\sum_{i=0}^{N_r}\left(\frac{O_{r_i}-P_{r_i}}{\sigma_{r_i}}\right)^2 + \frac{p}{N_s}\sum_{j=0}^{N_s}\left(\frac{O_{s_j}-P_{s_j}}{\sigma_{s_j}}\right)^2$$

where,

O_{r_i} observed receiver function at time t_i
P_{r_i} predicted receiver function at time t_i

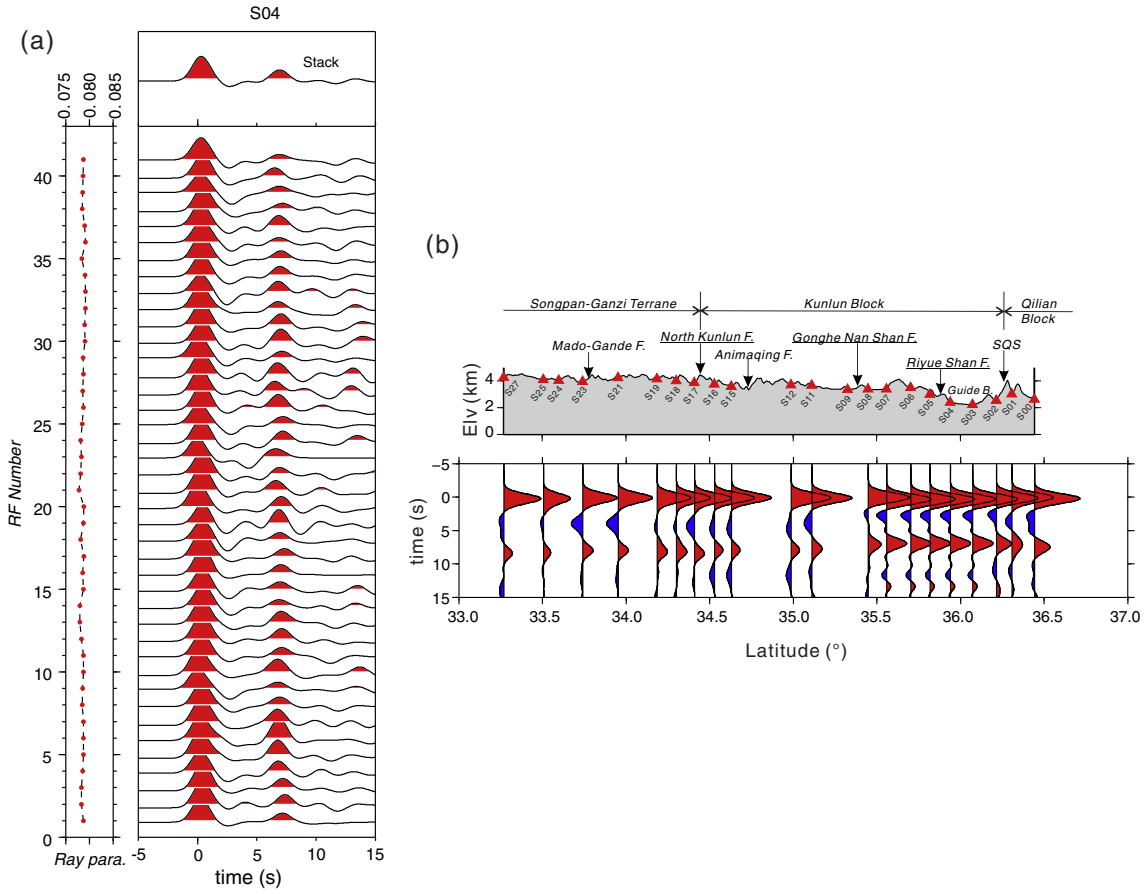

Fig. 7. (a) Receiver functions calculated at the station S04 basing on the selected teleseismic events. The left panel shows the corresponding ray parameters. (b) Stacked receiver functions with the Gaussian coefficient 1.0 for all available stations along the survey line from south to north. The signals at ~7–8 s depict the Moho signature.

σ_{r_i}	standard error of observation at t_i
O_{s_j}	jth observed surface wave phase velocity
P_{s_j}	jth predicted surface wave phase velocity
σ_{s_i}	standard error of jth surface wave phase velocity
N_r	total number of receiver function points
Ns	total number of surface wave phase velocity points
p	data weighting factor: $0 \le p \le 1$.

The parameter p controls the weight of two data sets in the joint inversion. In practice, considering that the Rayleigh wave phase velocities at periods from 5 to 20 s are mainly sensitive to the upper-middle crustal structure, we first set $p = 0$ thus forcing the solution to be exclusively based on the receiver functions, and use a damping factor 10 to avoid an overshoot of the firstly determined model. Then, we take both data sets by changing the weight $p = 0.2$ to allow both of them to participate in the inversion. The damping factor is also revised to 0.1. In this way, both data sets are fitted simultaneously during the inversion process. Since the periods of phase velocities are too short to constrain the middle-to-lower crustal structure well, we gradually decrease the weight of each layer from 1.0 to 0.1 as the depth increases from 30 km to 50 km, and no weight is applied to layers with depths above 50 km.

5.2. Inversion results

The inversion results for the stations S04 and S16 are shown in Fig. 8. The synthetic receiver functions based on the inversion results (red curves) have really high correlation coefficients of 0.9092 and 0.9522 with the observed receiver functions, respectively. The theoretical dispersion curves (continuous red lines) calculated from the inversion results also fit the observed phase velocities (dotted lines) well. In Fig. 9b, we show the shear-wave velocity image of the crust along the survey line. For comparison, the initial shear-wave velocity model derived from the study of Yang et al. (2012) is also shown in Fig. 9a. In order to check the reliability of the inversion results, we change the layer thickness of the initial model to 2 km and 2.5 km, and the inversion results shown in Fig. 10 are also very similar.

6. Discussion and conclusion

In view of the inversion result, the variation of the shear-wave velocities in the upper crust along the survey line is consistent with the Rayleigh wave phase velocities (Fig. 6). Low phase velocities at 5–17 s periods are obtained at the south of the Kunlun fault, and low shear-wave velocities at depths up to ~20 km are observed correspondingly at the same location. This can be attributed to the Middle to Late Triassic Songpan–Ganzi complex, with an estimated stratigraphic thickness of 10 km and reaching 15 km locally (Weislogel, 2008). At the north part of the survey line, low shear-wave velocities underlie the intramontane Guide basin, probably due to the Cenozoic fill and scattered Neogene/Quaternary deposits, or the tectonic destruction of upper crust from the Riyue Shan fault and South Qilan suture to the surrounding regions. Strike-slip faults mainly develop in the region south of Kunlun fault, such as Mado–Gande fault, and thrust faults develop north of the Kunlun fault, such as Animaqing, Gonghe Nan Shan, Laji Shan, and Qinghai Nan Shan. Considering lateral variations of the upper-crustal shear-wave velocity and the surface tectonic features along the survey line, we suggest that the upper-crustal properties between Songpan–Ganzi block and Kunlun block are probably different:

Please cite this article as: Wu, Z., et al., Crustal shear-wave velocity structure of northeastern Tibet revealed by ambient seismic noise and receiver functions, Gondwana Research (2015), http://dx.doi.org/10.1016/j.gr.2015.08.009

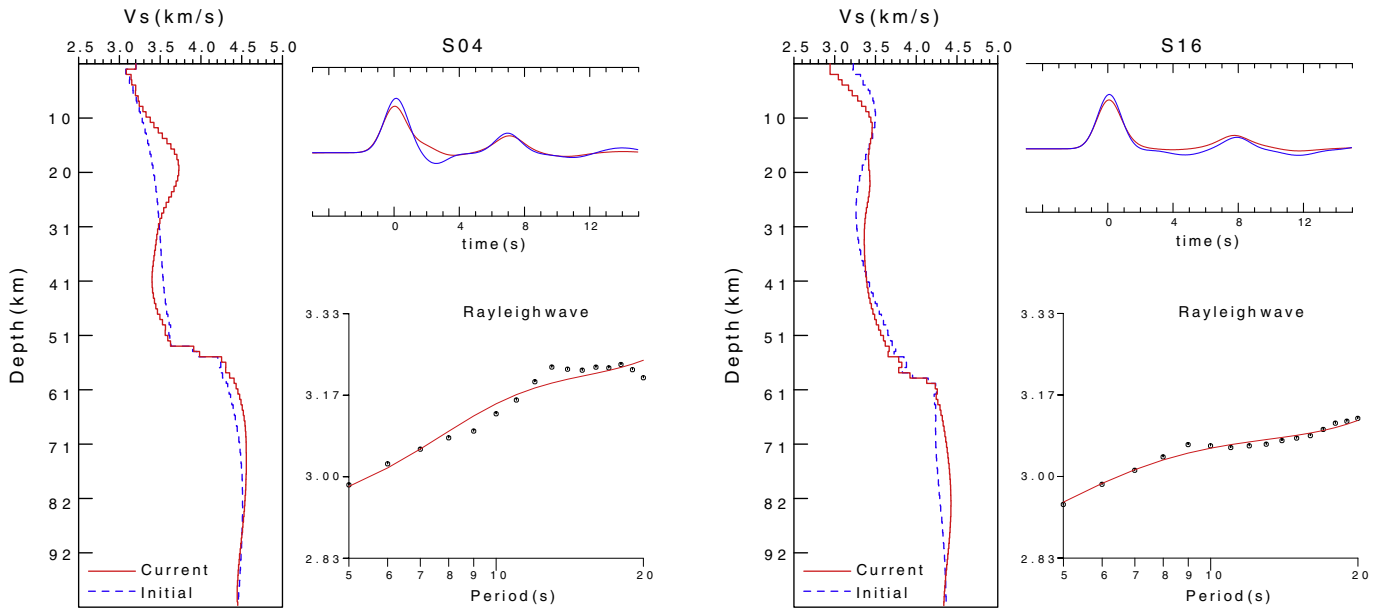

Fig. 8. 1-D shear-wave velocity inversion results for the stations S04 and S16. For both of them, we show the initial shear-wave velocity model (blue dashed line) and the inversion result (red line) on the left velocity–depth panel. On the right the upper panel shows the observed receiver function (blue curve) and the synthetic result from the inversion model (red curve) with the correlation coefficients 0.9092 and 0.9522, respectively. The lower panel shows the measured Rayleigh-wave phase velocities (black circle) and the synthetic result (red line). (For interpretation of the references to color in this figure legend, the reader is referred to the web version of this article.)

the upper crust in the Songpan–Ganzi block is more ductile, and in the Kunlun block shows more brittle feature.

There is an obvious phenomenon in the shear-wave velocity structure, that is, a low velocity zone (LVZ) is found in the middle-to-lower crust within the depth range about 40–60 km beneath the Songpan–Ganzi block. The mechanism that causes this LVZ is an important issue. The P-wave velocity model from the active-source seismic study (Zhang et al., 2011) shows that the P-wave velocity gradient agrees well with the average continental crust in the Songpan–Ganzi block, but the absolute value is lower by 0.5 km/s than the continental average. There are two possible explanations for this observation provided by Zhang et al. (2011). One is that the crust of the Songpan–Ganzi block is more felsic than normal crustal composition; if true, the average crustal *Vp*/*Vs* ratio should become lower than normal values. The other reason is related to the crustal temperature beneath the Songpan–Ganzi block, which needs to be 500 °C above the typical continental geothermal curves (Christensen, 1979). If so, the crustal *Vp*/*Vs* ratio should be much higher than 1.73 since the *Vs* values would be significantly smaller. The average crustal *Vp*/*Vs* in the Songpan–Ganzi block is ~1.81 provided by the previous receiver function study (Xu et al.,

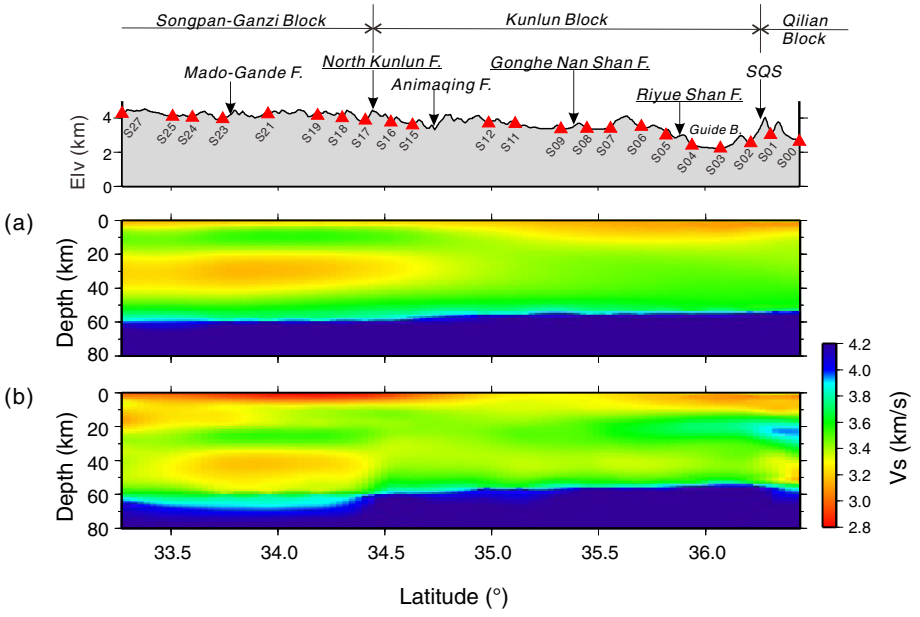

Fig. 9. On top: surface topography along the survey line and geographic locations of the broad-band stations (red triangles). The faults in Fig. 1b are added. (a) The initial shear-wave velocity model with the layer thickness 1.0 km provided by Yang et al. (2012). (b) Shear-wave velocity image of the crust along the study line based on the joint inversion of the Rayleigh-wave phase velocity dispersion and receiver functions. (For interpretation of the references to color in this figure legend, the reader is referred to the web version of this article.)

Please cite this article as: Wu, Z., et al., Crustal shear-wave velocity structure of northeastern Tibet revealed by ambient seismic noise and receiver functions, Gondwana Research (2015), http://dx.doi.org/10.1016/j.gr.2015.08.009

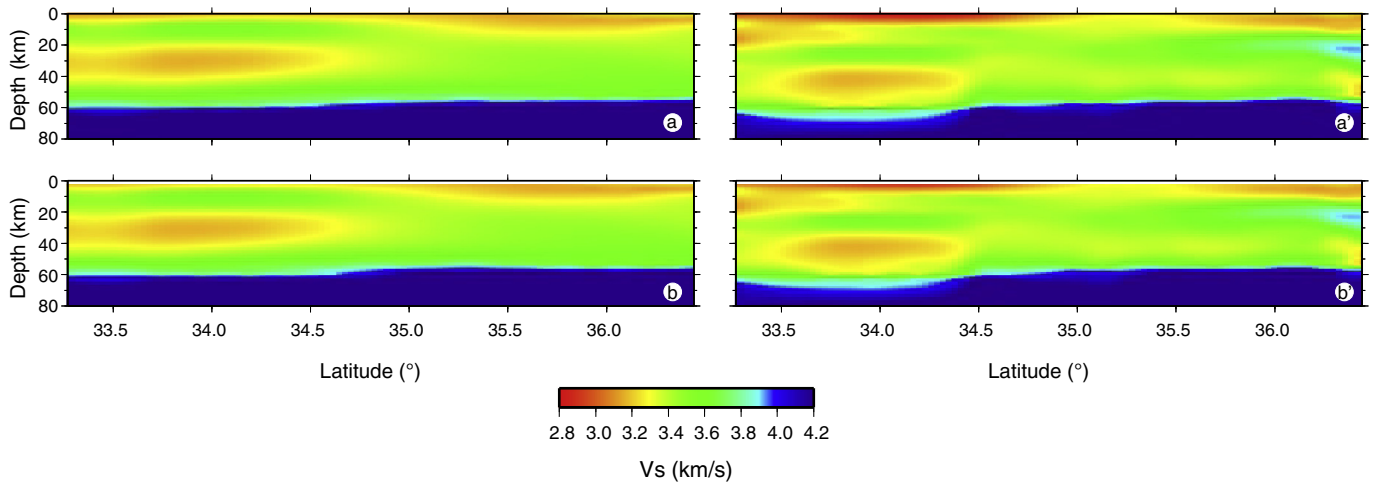

Fig. 10. Similar as Fig. 9 but with the layer thickness changed to 2 km (top) and 2.5 km (bottom), respectively. ⓐ - ⓐ' correspond to the initial model with the layer thickness 2 km and the joint inversion result. ⓑ - ⓑ' correspond to the initial model with the layer thickness 2.5 km and the joint inversion result.

2014), which is higher than 1.73 at stations S17–S27. All these observations are located in the Songpan–Ganzi block (Fig. 1b). Considering the high average crustal *Vp*/*Vs* ratio and corresponding high temperature in the crust here, the LVZ in the middle-to-lower crust beneath the Songpan–Ganzi block probably resulted from partial melting.

Several previous studies performed in the northeastern Tibetan plateau have found the existence of the LVZ, but the distribution areas are still obscure. Unsworth et al. (2004) report the existence of widespread fluids at depths 25–50 km in the region 32.5°N–35.5°N and 92°E–94°E. Later, Karplus et al. (2013) extend this region to 32°N–36°N and 92°E–98°E by means of low group velocities found at periods 34–40 s, which are sensitive to the middle-to-lower crust velocity at depths of ~30–60 km. Yang et al. (2012) observe low velocities in a range of 2.9 to 3.3 km/s at depths 20–40 km in the Songpan–Ganzi block and suggest that the reason is partial melting. Two recent studies based on ambient noise surface wave tomography show a prominent LVZ in the middle crust of the Songpan–Ganzi block at depths 20–40 km (H.Y. Li et al., 2014; X.F. Li et al., 2014). These studies show that the LVZ in the NE Tibetan plateau only exists in the region south of the North Kunlun fault, but Jiang et al. (2014) suggest that the LVZ in the NE Tibetan plateau is confined to the region south of the Kunlun fault and west of 98°E, and it penetrates northward into the Qinling orogens to the region north of the Kunlun fault and east of 98°E. In our shear-wave velocity structure, we do not observe LVZ under the Kunlun block north of Kunlun fault. This difference may reflect intrinsic variations of two blocks before their collision, or it is because the Kunlun fault limits the northward extension of the LVZ. According to all the observations, the north limit of the LVZs in the NE Tibetan plateau probably distributes non-uniformly in different regions and more studies need to investigate its distribution in detail.

The LVZ in the northeastern Tibetan plateau is comparable to that in other parts of the plateau, such as the eastern, central and southern Tibet. Geophysical studies using different methods also find high electrical conductivity, high temperature and low strength zones with low seismic velocities in the middle-to-lower crust beneath the plateau (e.g. Clark and Royden, 2000; Yao et al., 2008; Guo et al., 2009; Li et al., 2009; Zheng et al., 2010; Yang et al., 2012; Zheng et al., 2013; Liu et al., 2014). The effects of this LVZ on the dynamic mechanism and deformation of the NE Tibetan plateau are still controversial topics. Clark and Royden (2000) propose the channel flow model to explain the surface topography of the surrounding regions of the Tibetan plateau. To the east, they suggest that the adjacent crust of the Sichuan Basin is mechanically weak, and the middle-to-lower crust of the plateau can escape to these regions, thus producing the broader plateau margin with a smoother topographic gradient. Yang et al. (2012) point that the LVZ observed in the middle-to-lower crust only based on Rayleigh wave observations is not strong enough to support the argument of the channel flow model. Liu et al. (2014) conclude that the eastward extension of the Tibetan plateau is accommodated by a combination of local crustal flow and strain partitioning across deep faults such as the Longmen Shan fault, and propose that rigid block motion and crustal flow may be reconcilable as mutual modes in the framework of crustal deformation in southeastern Tibet. In order to determine whether the channel flow model could dominantly explain the tectonic process in the NE Tibetan plateau, we should perform more work in the future such as accurate Love wave phase velocity measurements for radial anisotropy, inversion of azimuthal anisotropy, and investigation of lithospheric shear-wave velocities in this region.

Acknowledgments

We want to bring here the memory of Prof. Zhongjie Zhang, who until recently was the leader of the research group in the IGGCAS and also our dear friend, who unexpectedly passed away on September 6th, 2013 at the early age of 49 years old. It was Zhongjie who led, together with other colleagues, most of the fieldworks and research projects in Tibet, including the deployment of the seismic array used in this study. We are thankful to Prof. Robert Herrmann, Saint Louis University, for providing us the computer software package, and Prof. Xiaobo Tian, and Dr. Yun Chen and Xiaofeng Liang for their kind help on this research work. We are also thankful for the constructive criticisms from anonymous reviewers for helping us to improve this paper. We gratefully acknowledge the financial support for this work contributed by the Chinese Academy of Sciences (XDB03010700), the China Earthquake Administration (201408023), the National Natural Science Foundation of China (41174075 and 41474068) and the Fundamental Research Funds for the Central Universities (WK2080000053).

References

Aitchison, J.C., Xia, X., Baxter, A.T., Ali, J.R., 2011. Detrital zircon U–Pb ages along the Yarlung–Tsangpo suture zone, Tibet: implications for oblique convergence and collision between India and Asia. Gondwana Research 20, 691–709.

Ammon, C.J., Randall, G.E., Zandt, G., 1990. On the nonuniqueness of receiver function inversions. Journal of Geophysical Research 95, 15,303–15,318.

Badal, J., Chen, Y., Chourak, M., Stankiewicz, J., 2013. S-wave velocity images of the Dead Sea Basin provided by ambient seismic noise. Journal of Asian Earth Sciences 75, 26–35.

Bensen, G.D., Ritzwoller, M.H., Barmin, M.P., Levshin, A.L., Lin, F., Moschetti, M.P., Shapiro, N.M., Yang, Y., 2007. Processing seismic ambient noise data to obtain reliable broad-band surface wave dispersion measurements. Geophysical Journal International 169, 1239–1260.

Burchfiel, B.C., Chen, Z., Liu, Y., Royden, L.H., 1995. Tectonics of the Longmenshan and adjacent regions. International Geology Review 37, 661–735.

Chen, Y., Li, W., Yuan, X., Badal, J., Teng, J., 2015. Tearing of the Indian lithospheric slab beneath southern Tibet revealed by SKS-wave splitting measurements. Earth and Planetary Science Letters 413, 13–24.

Christensen, N.I., 1979. Compressional wave velocities in rocks at high temperatures and pressures, critical thermal gradients, and crustal low-velocity zones. Journal of Geophysical Research 84, 6489–6857.

Clark, M.K., Royden, L.H., 2000. Topographic ooze: building the eastern margin of Tibet by lower crustal flow. Geology 28 (8), 703–706.

Clark, M.K., Farley, K.A., Zheng, D.W., Wang, Z.C., Duvall, A.R., 2010. Early Cenozoic faulting of the northern Tibetan Plateau margin from apatite (U–Th)/He ages. Earth and Planetary Science Letters 296, 78–88.

Dai, S., Fang, X.M., Dupont-Nivet, G., Song, C.H., Gao, J.P., Krijgsman, W., Langereis, C., Zhang, W.L., 2006. Magnetostratigraphy of Cenozoic sediments from the Xining Basin: tectonic implications for the northeastern Tibetan Plateau. Journal of Geophysical Research 111, B11102.

Deng, Y.F., Shen, W., Xu, T., Ritzwoller, M.H., 2015. Crustal layering in northeastern Tibet: a case study on joint inversion of receiver functions and surface wave dispersion. Geophysical Journal International 203, 692–706.

Duvall, A.R., Clark, M.K., 2010. Dissipation of fast strike-slip faulting within and beyond northeastern Tibet. Geology 38 (3), 223–226.

England, P., Houseman, G., 1986. Finite strain calculations of continental deformation. 2. Comparison with the India–Asia collision zone. Journal of Geophysical Research 91 (B3), 3664–3676.

England, P., Houseman, G., 1989. Extension during continental convergence with application to the Tibetan plateau. Journal of Geophysical Research 94 (B12), 17,561–17,579.

Enkelmann, E., Weislogel, A., Ratschbacher, L., Eide, E., Renno, A., Wooden, J., 2007. How was the Triassic Songpan–Ganzi basin filled? A provenance study. Tectonics 26, TC4007. http://dx.doi.org/10.1029/2006TC002078.

Fang, X.M., Yan, M., der Voo, R.V., Rea, D.K., Song, C.H., 2005. Late Cenozoic deformation and uplift of the NE Tibetan Plateau: evidence from high-resolution magnetostratigraphy of the Guide Basin, Qinghai Province, China. GSA Bulletin 117, 1208–1225.

Fu, B.H., Awata, Y., 2007. Displacement and timing of left-lateral faulting in the Kunlun Fault Zone, northern Tibet, inferred geologic and geomorphic features. Journal of Asian Earth Sciences 29, 253–265.

Galvé, A., Hirn, A., Jiang, M., Gallart, J., de Voogd, B., Lepine, J.C., Diaz, J., Wang, Y.X., Qian, H., 2002. Modes of raising northeastern Tibet probed by explosion seismology. Earth and Planetary Science Letters 203, 35–43.

Guo, Z., Gao, X., Yao, H.J., Li, J., Wang, W.M., 2009. Mid crustal low-velocity layer beneath the central Himalaya and southern Tibet revealed by ambient noise array tomography. Geochemistry, Geophysics, Geosystems 10, Q05007. http://dx.doi.org/10.1029/2009GC002458.

Herrmann, R.B., Ammon, C.J., 2004. Surface Waves, Receiver Functions and Crustal Structure. Computer Programs in Seismology, Version 3.30. Saint Louis University (http://www.eas.slu.edu/PeopleRBHerrmann/CPS330.html).

Hu, X.M., Wang, J.G., BouDagher-Fadel, M., Garzanti, E., 2015. New insights into the timing of the India–Asia collision from the Paleogene Quxia and Jialazi Formations of the Xigaze forearc basin, South Tibet. Gondwana Research http://dx.doi.org/10.1016/j.gr.2015.02.007.

Jiang, M., Galvé, A., Hirn, A., de Voogd, B., Laigle, M., Su, H.P., Diaz, J., Lépine, J.C., Wang, Y.X., 2006. Crustal thickening and variations in architecture from the Qaidam basin to the Qang Tang (North-Central Tibetan Plateau) from wide-angle reflection seismology. Tectonophysics 412, 121–140.

Jiang, C.X., Yang, Y.J., Zheng, Y., 2014. Penetration of mid-crustal low velocity zone cross the Kunlun Fault in the NE Tibetan Plateau revealed by ambient noise tomography. Earth and Planetary Science Letters 406, 81–92.

Julià, J., Ammon, C.J., Herrmann, R.B., Correig, A.M., 2000. Joint inversion of receiver function and surface wave dispersion observations. Geophysical Journal International 143 (1), 99–112.

Karplus, M.S., Klemperer, S.L., Lawrence, J.F., Zhao, W., Mechie, J., Tilmann, F., Sandvol, E., Ni, J., 2013. Ambient-noise tomography of north Tibet limits geological terrane signature to upper-middle crust. Geophysical Research Letters 40, 808–813.

Kind, R., Yuan, X., Saul, J., Nelson, D., Sobolev, S.V., Mechie, J., Zhao, W., Ni, J., Achauer, U., Jiang, M., 2002. Seismic images of crust and upper mantle beneath Tibet: evidence for Eurasian plate subduction. Science 298, 1219–1221.

Li, H.Y., Su, W., Wang, C.Y., Huang, Z.X., 2009. Ambient noise Rayleigh wave tomography in western Sichuan and eastern Tibet. Earth and Planetary Science Letters 282, 201–211.

Li, H.Y., Shen, Y., Huang, Z.X., Li, X.F., Gong, M., Shi, D.N., Sandvol, E., Li, A.B., 2014a. The distribution of the mid-to-lower crustal low-velocity zone beneath the northeastern Tibetan Plateau revealed from ambient noise tomography. Journal of Geophysical Research, Solid Earth 119, 1954–1970.

Li, X.F., Li, H.Y., Shen, Y., Gong, M., Shi, D.N., Sandvol, E., Li, A.B., 2014b. Crustal velocity structure of the Northeastern Tibetan Plateau from ambient noise surface-wave tomography and its tectonic implications. Bulletin of the Seismological Society of America 104. http://dx.doi.org/10.1785/0120130019.

Ligorría, J.P., Ammon, C.J., 1999. Iterative deconvolution and receiver-function estimation. Bulletin of the Seismological Society of America 89, 1395–1400.

Liu, M.J., Mooney, W., Li, S.L., Okaya, N., Detweiler, S., 2006. Crustal structure of the northeastern margin of the Tibetan plateau from the Songpan–Ganzi terrane to the Ordos basin. Tectonophysics 420, 253–266.

Liu, Q.Y., van der Hilst, R.D., Li, Y., Yao, H.J., Chen, J.H., Guo, B., Qi, S.H., Wang, J., Huang, H., Li, S., 2014. Eastward expansion of the Tibet Plateau by crustal flow and strain partitioning across faults. Nature Geoscience 30, 361–365.

Meyer, B., Tapponnier, P., Bourjot, L., Métivier, F., Gaudemer, Y., Peltzer, G., Shunmin, G., Zhitai, C., 1998. Crustal thickening in Gansu–Qinghai, lithospheric mantle subduction, and oblique, strike-slip controlled growth of the Tibet plateau. Geophysical Journal International 135, 1–47.

Molnar, P., Tapponnier, P., 1975. Cenozoic tectonics of Asia: effects of a continental collision. Science 189, 419–426.

Montagner, J.P., 1986. Regional three-dimensional structures using long period surface waves. Geophysicae 4, 283–294.

Pape, F.L., Jones, A.G., Vozar, J., Wei, W.B., 2012. Penetration of crustal melt beyond the Kunlun Fault into northern Tibet. Nature Geoscience 5, 330–335.

Replumaz, A., Capitanio, F.A., Guillot, S., Negredo, A.M., Villaseñor, A., 2014. The coupling of Indian subduction and Asian continental tectonics. Gondwana Research 26, 608–626.

Rowley, D.B., 1996. Age of initiation of collision between India and Asia a review of stratigraphic data. Earth and Planetary Science Letters 145, 1–13.

Royden, L.H., Burchfiel, B.C., King, R.W., Wang, E.C., Chen, Z.L., Shen, F., Liu, Y.P., 1997. Surface deformation and lower crustal flow in Eastern Tibet. Science 276, 788–790.

Shapiro, N.M., Campillo, M., Stehly, L., Ritzwoller, M.H., 2005. High-resolution surface wave tomography from ambient seismic noise. Science 307, 1615–1618.

Stehly, L., Campillo, M., Shapiro, N.M., 2006. A study of the seismic noise from its long-range correlation properties. Journal of Geophysical Research 111, B10306.

Sun, Z., Pei, J., Li, H., Xu, W., Zhu, Z., Wang, X., Yang, Z., 2012. Palaeomagnetism of late Cretaceous sediments from southern Tibet: evidence for the consistent palaeolatitudes of the southern margin of Eurasia prior to the collision with India. Gondwana Research 21, 53–63.

Tapponnier, P., Molnar, P., 1976. Slip-line field theory and large-scale continental tectonics. Nature 264 (25), 319–324.

Tapponnier, P., Peltzer, G., Dain, A.Y., Armijo, R., 1982. Propagating extrusion tectonics in Asia: new insights from simple experiments with plasticine. Geology 10, 611–616.

Tapponnier, P., Xu, Z., Roger, F., Meyer, B., Arnaud, N., Wittlinger, G., Yang, J., 2001. Oblique stepwise rise and growth of the Tibet plateau. Science 294, 1671–1677.

Tarantola, A., Valette, B., 1982. Generalized nonlinear inverse problem solved using the least squares criterion. Reviews of Geophysics and Space Physics 20 (2), 219–232.

Tian, X.B., Zhang, Z.J., 2013. Bulk crustal properties in NE Tibet and their implications for deformation model. Gondwana Research 24, 548–559.

Unsworth, M., Wei, W.B., Jones, A.G., Li, S.H., Bedrosian, P., Booker, J., Sheng, J., Ming, D., Tan, H.D., 2004. Crustal and upper mantle structure of northern Tibet imaged with magnetotelluric data. Journal of Geophysical Research 109, B02403. http://dx.doi.org/10.1029/2002 JB002305.

Vergne, J., Wittlinger, G., Hui, Q., Tapponnier, P., Poupinet, G., Mei, J., Herquel, G., Paul, A., 2002. Seismic evidence for stepwise thickening of the crust across the NE Tibetan plateau. Earth and Planetary Science Letters 203, 25–33.

Villaseñor, A., Yang, Y., Ritzwoller, M.H., Gallart, J., 2007. Ambient noise surface wave tomography of the Iberian Peninsula: implications for shallow seismic structure. Geophysical Research Letters 34, L11304. http://dx.doi.org/10.1029/2007GL030164.

Weislogel, A.L., 2008. Tectonostratigraphic and geochronologic constraints on evolution of the northeast Paleotethys from the Songpan–Ganzi Complex, central China. Tectonophysics 451, 331–345.

Xia, L., Liu, X., Ma, Z., Xu, X., Xia, Z., 2011. Cenozoic volcanism and tectonic evolution of the Tibetan plateau. Gondwana Research 19, 850–866.

Xu, T., Wu, Z.B., Zhang, Z.J., Tian, X.B., Deng, Y.F., Wu, C.L., Teng, J.W., 2014. Crustal structure across the Kunlun fault from passive source seismic profiling in East Tibet. Tectonophysics 627, 98–107.

Yang, Y.J., Ritzwoller, M.H., Levshin, A.L., Shapiro, N.M., 2007. Ambient noise wave tomography across Europe. Geophysical Journal International 168, 259–274.

Yang, Y.J., Ritzwoller, M.H., Zheng, Y., Shen, W.S., Levshin, A.L., Xie, Z.J., 2012. A synoptic view of the distribution and connectivity of the mid-crustal low velocity zone beneath Tibet. Journal of Geophysical Research 117, B04303. http://dx.doi.org/10.1029/2011JB008810.

Yao, H.J., van der Hilst, R.D., de Hoop, M.V., 2006. Surface-wave array tomography in SE Tibet from ambient seismic noise and two-station analysis: I— phase velocity maps. Geophysical Journal International 166, 732–744.

Yao, H.J., Beghein, C., van der Hilst, R.D., 2008. Surface-wave array tomography in SE Tibet from ambient seismic noise and two-station analysis: II— crustal and upper-mantle structure. Geophysical Journal International 173, 205–219.

Yao, H.J., van der Hilst, R.D., Montagner, J.-P., 2010. Heterogeneity and anisotropy of the lithosphere of SE Tibet from surface wave array tomography. Journal of Geophysical Research 115, B12307. http://dx.doi.org/10.1029/2009JB007142.

Yin, A., Harrison, T.M., 2000. Geologic evolution of the Himalayan–Tibetan orogen. Annual Review of Earth and Planetary Sciences 28, 211–280.

Yu, S.Y., Zhang, J.X., Real, P.G.D., 2012. Geochemistry and zircon U–PB ages of adakitic rocks from the Dulan area of the North Qaidam UHP terrane, north Tibet: constraints on the timing and nature of regional tectonothermal events associated with collisional orogeny. Gondwana Research 21, 167–179.

Yuan, D.Y., Champagnac, J.D., Ge, W.P., Molnar, P., Zhang, P.Z., Zheng, W.J., Zhang, H.P., Liu, X.W., 2011. Late Quaternary right-lateral slip rates of faults adjacent to the lake Qinghai, northeastern margin of the Tibetan Plateau. GSA Bulletin 123 (9/10), 2016–2030.

Zhang, Z.J., Yuan, X.H., Chen, Y., Tian, X.B., Kind, R., Li, X.Q., Teng, J.W., 2010. Seismic signature of the collision between the east Tibetan escape flow and the Sichuan Basin. Earth and Planetary Science Letters 292, 254–264.

Please cite this article as: Wu, Z., et al., Crustal shear-wave velocity structure of northeastern Tibet revealed by ambient seismic noise and receiver functions, Gondwana Research (2015), http://dx.doi.org/10.1016/j.gr.2015.08.009

Zhang, Z.J., Klemperer, S., Bai, Z.M., Chen, Y., Teng, J.W., 2011. Crustal structure of the Paleozoic Kunlun orogeny from an active-source seismic profile between Moba and Guide in East Tibet, China. Gondwana Research 19, 994–1007.
Zhang, J.J., Santosh, M., Wang, X.X., Guo, L., Yang, X.Y., Zhang, B., 2012. Tectonics of the northern Himalaya since the India–Asia collision. Gondwana Research 21, 939–960.
Zheng, Y., Yang, Y.J., Ritzwoller, M.H., Zheng, X.F., Xiong, X., Li, Z.N., 2010. Crustal structure of the northeastern Tibetan plateau, the Ordos block and the Sichuan basin from ambient noise tomography. Earthquake Science 23, 465–476.
Zheng, Y., Shen, W.S., Zhou, L.Q., Yang, Y.J., Xie, Z.J., Ritzwoller, M.H., 2011. Crust and uppermost mantle beneath the North China Craton, northeastern China, and the Sea of Japan from ambient noise tomography. Journal of Geophysical Research 116. http://dx.doi.org/10.1029/2011JB008637.
Zheng, Y., Can, G.E., Xie, Z.J., Yang, Y.J., Xiong, X., Hsu, H.T., 2013. Crustal and upper mantle structure and the deep seismogenic environment in the source regions of the Lushan earthquake and the Wenchuan earthquake. Science China Earth Sciences 56 (7), 1158–1168.

Please cite this article as: Wu, Z., et al., Crustal shear-wave velocity structure of northeastern Tibet revealed by ambient seismic noise and receiver functions, Gondwana Research (2015), http://dx.doi.org/10.1016/j.gr.2015.08.009